PAPER

Screening for electrically conductive defects in thin functional films using electrochemiluminescence

Received 00th January 20xx, Accepted 00th January 20xx

DOI: 10.1039/x0xx00000x

Harley Quinn,^a Wenlu Wang,^a Jörg G. Werner,^{ab} and Keith A. Brown*^{abc}

Multifunctional thin films in energy-related devices often must be electrically insulating where a single nanoscale defect can result in complete device-scale failure. Locating and characterizing such defects presents a fundamental problem where high-resolution imaging methods are needed to find defects, but imaging with high spatial resolution limits the field of view and thus the measurement throughput. Here, we present a novel high-throughput method for detecting sub-micron defects in insulating thin films by leveraging the electrochemiluminescence (ECL) of luminol. Through a systematic study of reagent concentrations, buffers, voltage, and excitation time, we identify optimized conditions at which it is possible to detect sub-micron defects at high-throughput. Extrapolating from the signal to background observed for detecting 440 nm wide lines and 620 nm diameter circles, we estimate the minimum detectable features to be lines as narrow as 2.5 nm in width and pinholes as small as 70 nm in radius. We further explore this method by using it to characterize a nominally insulating phenol film and find conductive defects that are cross-correlated with high-resolution atomic force microscopy to provide feedback to synthesis. Given this assay's inherent parallelizability and scalability, it is expected to have a major impact on the automated discovery of multifunctional films.

Introduction

Thin multifunctional films are ubiquitous in energy-related devices including fuel cells, 1 batteries, 2-6 and photovoltaics. 7,8 An essential requirement for such films is that they allow the transport of different species to be independently managed. For example, solid-state battery electrolyte films require that ions can readily pass through the film while electrons cannot. The requirement for electrical insulation is particularly insidious in the context of scalability because a single nanoscale defect in a device with square centimeters of functional area can critically impact device performance.3,4 Detecting the presence of a defect, for example, through leakage current or short circuits, is straightforward, but identifying its location is essential to determining its origin and finding synthesis and processing conditions that mitigate such defects. However, locating and characterizing defects presents a fundamental problem where high-resolution imaging methods are needed to find defects, but imaging with high spatial resolution typically comes with the tradeoff of limiting the field of view. Current techniques used for defect detection include direct inspection techniques such as atomic force microscopy (AFM)9-11 and scanning electron microscopy (SEM).11-13 In addition to these methods which identify defects through their structure, there are also methods for directly measuring defects through their functional

signature such as scanning electrochemical microscopy (SECM), which is a contactless and high-resolution method for measuring local electrochemical activity. ^{14–16} Early work showed that this method can be used to quantify film conductivity, ¹⁴ and then this was extended to a mapping approach to measure substrate conductivity across 800 µm wide regions. ¹⁵ However, two drawbacks of probe-based approaches are that data collection is a serial process and resolution is constrained by the ultramicroelectrode tip radius and the tip-sample separation, ¹⁶ making it challenging and prohibitively time consuming to map large regions at a fine resolution.

In contrast with methods for serially mapping the properties of functional films with spatial resolution commensurate with the defects of interest, when considering the identification and mapping of sparse microscopic defects on macroscopic samples, it would be preferable to amplify defects so that they can be rapidly identified with low-resolution tools. For example, the reductive growth of silver can amplify the optical signature of small defects,17 but it would be preferable to employ a method that is non-destructive so that further analysis could be performed once defects are located. Considering these requirements, optical methods that feature a dark-field readout where defects generate light have the advantages of being inherently parallelizable, compatible with low magnification imaging for large-area screening, and the lack of signal generated on correctly functioning films vastly facilitates signal analysis. Furthermore, conventional limitations of optical imaging, such as the diffraction limit, do not present a challenge when the goal is to make defects appear large. When considering a process for generating light using electrically

^a Division of Materials Science & Engineering, Boston University, Boston, MA, 02215, USA. E-mail: brownka@bu.edu

b. Department of Mechanical Engineering, Boston University, Boston, MA, 02215, USA

^{c.} Department of Physics, Boston University, Boston, MA, 02215, USA

conductive defects, the electrochemiluminescence (ECL) of luminol stands out as a widely used method. ^{18–24} In addition to its widespread use in forensics and biology, ^{18–21} it has also been used to map ECL on surfaces, ²² quantify variations in catalytic activity, ²³ and even facilitate the readout of human fingerprints. ²⁴ However, the use of luminol-based ECL to explore conductive defects on nominally insulating films has not been shown and there are open questions about the role of processing conditions and what resolving power and throughput can be achieved using this method.

Here, we show that luminol ECL can be used to map nanoscale conductive defects on nominally insulating films. Specifically, we explore the hypothesis that applying a potential across a sandwiched electrochemical cell will result in the localized emission of light on exposed regions of the anode (Figure 1A). To turn this hypothesis into an assay, we first perform a systematic study of the ECL conditions including reagent concentrations, properties of the buffer, excitation voltage, and excitation duration. Interestingly, these factors

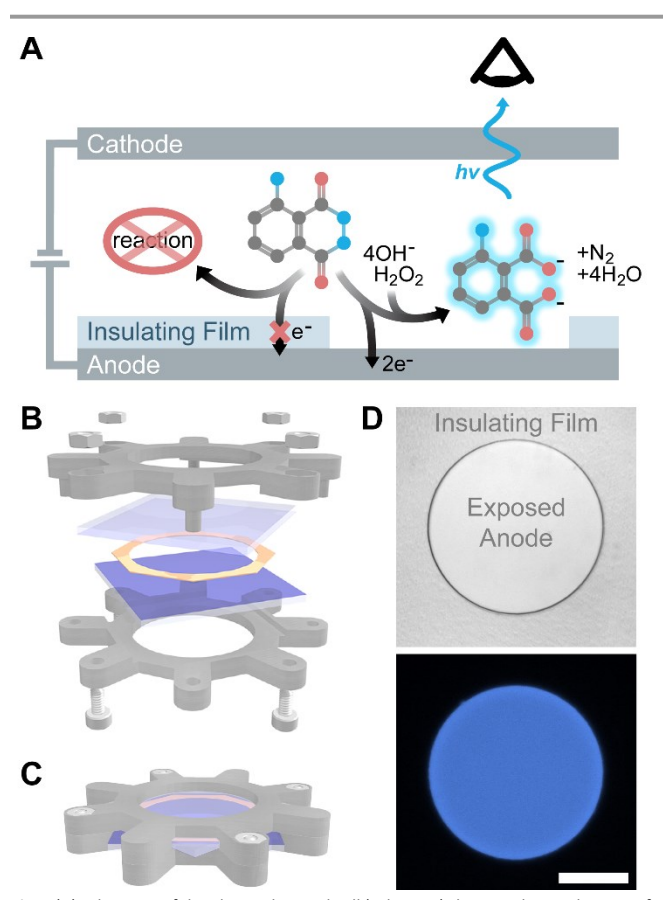


Fig. 1 (A) Schematic of the electrochemical cell (side view) showing the mechanism of luminol electrochemiluminescence (ECL). (B) Exploded view of electrochemical cell and holder (grey) with screws and nuts (light grey), glass slides (light blue) with ITO coating (medium blue), and spacer (gold). (C) Assembled electrochemical cell. (D) Optical micrographs through the electrochemical cell showing a region of the anode in which a 500 μ m diameter circular region is exposed while the rest of the anode is protected by an insulating film. Here, the electrochemical cell was filled with 1 mM luminol, 5 mM H₂O₂ pH 12 NaOH solution. The top image shows the region when illuminated externally while the bottom image shows the same region without external illumination but with the exposed anode luminescing through ECL upon the application of a 1.6 V potential across the cell for 2 s. The bottom image was taken in greyscale and false-colored to represent the color seen by eye. Scale bar is 200 μ m.

have a subtle interplay with a decrease in ECL occurring at excessive voltages, durations, or luminol concentrations. Then, with this optimization in hand, we perform a study of the ECL signal originating from nanoscale dot and line defects and are able to resolve 440 nm wide lines with >150 signal to background ratio and 620 nm diameter circles with ~20 signal to background ratio. Using this information, we predict that it should be possible to detect lines as narrow as 2.5 nm in diameter and circles as small as 70 nm in radius. Finally, we employ this assay to map a number of conductive defects on an electrodeposited ultrathin poly(phenylene oxide) film and show that these can be colocalized with AFM as a higher-resolution technique. Collectively, these experiments show that luminol ECL provides a rapid and parallelizable way of observing defects and providing feedback for the development of advanced multifunctional films.

Experimental

Reagents

All reagents were used as purchased without further purification. For the buffer screening experiment, four buffers were prepared (1) 18 mM sodium borate (ACS grade, ≥99.5%, Sigma-Aldrich) adjusted to pH 10, (2) 41 mM sodium bicarbonate (ACS grade, Fisher Chemical) adjusted to pH 10, (3) 35 mM sodium bicarbonate adjusted to pH 11, and (4) 33 mM disodium phosphate (ACS grade, ≥99.0%, Alfa Aesar) adjusted to pH 12. All buffers were pH adjusted by adding quantities of 100 mM sodium hydroxide (BioXtra, ≥98.0%, Sigma-Aldrich) solution. Luminol sodium salt (≥98%, Sigma-Aldrich) was dissolved in the appropriate buffer for each experiment to reach a concentration of 100 mM luminol to make stock solutions which were stored at 5 °C. Working solutions were prepared the same day of experiments by diluting the stock solution with the same buffers and adding hydrogen peroxide immediately prior to use. After buffer screening experiments were completed, a pH 11 sodium bicarbonate buffer was used to prepare a stock solution which was then aliquoted and stored at -18 °C for all subsequent experiments. Working solutions were prepared the same day of experiments by thawing the stock solution, diluting with buffer, and adding hydrogen peroxide immediately prior to

Polymethyl methacrylate (PMMA) electron-beam resist (1000 HARP eB 0.3, KemLab), hydrogen peroxide solution 30% w/w in H₂O (29.0 - 32.0%, Sigma), Microposit MF-319 developer (Rohm and Hass), Microposit S1813 G2 positive photoresist (electronic grade, Rohm and Hass), sodium tetraborate decahydrate (ACS grade, ≥99.5%, Sigma), acetone (semi grade, VWR Chemicals), 2-propanol (semi grade, VWR Chemicals), acetonitrile (anhydrous, Fisher Scientific), tetramethylammonium hydroxide pentahydrate (TMAH, ≥97%, Sigma-Aldrich), tetrabutylammonium perchlorate (TBAP, ≥97.5%, Fisher Scientific), silver perchlorate (anhydrous, Fisher Scientific), and diethyl ether (anhydrous, Sigma-Aldrich) were used as received. Developer for the HARP PMMA e-beam resist was prepared by mixing methyl isobutyl ketone (MiBK,

microelectronic grade, J.T.Baker) and 2-propanol (IPA, microelectronic grade, J.T.Baker) in a 1:3 ratio v/v.

Substrate preparation

Microscale experiments

Indium tin oxide (ITO)-coated glass slides ($25 \times 25 \times 1.1 \text{ mm}^3$, surface resistivity $70-100~\Omega/\text{sq}$, part number 703176-Sigma Aldrich) were coated with Microposit S1813 G2 positive photoresist using a Headway Research spinner (PWM32) at 4,000 rpm resulting in a resist thickness between 1 and 1.5 μ m. A series of circles (diameters between 100 and 1500 μ m) was patterned onto each slide using a Karl Suss MA6 mask aligner to define multiple separated regions of exposed ITO on one substrate.

Nanoscale experiments

ITO-coated glass slides were coated with 1000 HARP PMMA ebeam resist (eB 0.3, KemLab) using a Headway Research spinner (PWM32) at 4,000 rpm resulting in a resist thickness between 0.2 and 0.3 μm. A series of lines (between 0.1 and 1 μm wide) or circles (diameters between 0.1 and 1 µm) were patterned onto the slide using a Zeiss Supra 40VP field emission scanning electron microscope (FE-SEM) with a Nanometer Pattern Generation System (NPGS, JC Nabity Lithography Systems) to define multiple separated regions of exposed ITO on one substrate. Lines were designed to be 50 μm long and spaced by $75\,\mu m$ in the narrow dimension and $50\,\mu m$ in the long dimension. Circles were positioned in columns that were 75 μm apart and rows that were 100 µm apart. A grid of samples was prepared with exposure doses between 150 and 3000 $\mu C/cm^2$, but analysis of ECL focused on a single dose and all studied features were interrogated in a single ECL experiment using 5× magnification. After ECL experiments were performed, the feature sizes were verified using the same FE-SEM with an inlens detector. A moderate accelerating voltage of 4.40 kV was chosen to mitigate sample charging.

Phenol film synthesis

Electrodeposition of an ultrathin layer of dielectric poly(phenylene oxide) onto ITO-coated glass slides was performed in 10 mM acetonitrile. A stoichiometric ratio of TMAH was used to form the oxidizable phenolate with 100 mM TBAP as the supporting electrolyte. For the deposition, a three-electrode system was used with ITO as the working electrode, a platinum wire as the counter electrode, and Ag/Ag⁺ as the reference electrode. The reference electrode was composed of a silver wire in 0.05 M silver perchlorate and 0.1 M TBAP in acetonitrile and separated from the monomer solution by a Gamry glass frit. Chronoamperometry (CA) was conducted on the solution at 0.1 V vs. Ag/Ag⁺ for 20 minutes using a Gamry Reference 600+ potentiostat. After deposition, the film was cleaned with pure acetonitrile followed by diethyl ether.

ECL imaging procedure

A working solution composed of 3.2 mM luminol, 5.6 mM H_2O_2 , in a sodium bicarbonate buffer (35 mM, pH 11) was used in the experiments shown in Figures 3, 4, and 5. For the experiments shown in Figure 2, different luminol concentrations, peroxide concentrations, and buffer compositions were explored. First, a

fluid cell was constructed by placing a laser-cut polyimide spacer (part 2271K72 - McMaster) with a thickness of $177 \pm 1 \,\mu m$ onto an ITO-coated slide with a polymer coating. Then, the ITO-coated slide was placed into a 3D-printed mounting (printed using a FormLabs Form2 out of grey resin). Next, 10 µL of the working solution was pipetted onto the center of the slide. Finally, an additional ITO-coated slide, with no polymer coating, was placed into a second 3D-printed mounting and this assembly was combined with the first mounted slide to form a fluid cell.²⁵ The fluid cell is shown in an exploded-view in Figure 1B and assembled in Figure 1C. After assembly, this fluid cell was secured under an Olympus BX43 optical microscope with a Hamamatsu ORCA-R2 digital camera C10600 and a dark-field filter cube. This provided a direct view of the patterned electrode surface through the fluid cell (Figure 1D).

An Arduino Uno was used to define the timing of the ECL experiments. In particular, it sourced one timed DC voltage to initiate image capture and a subsequent DC signal that was routed through an analog filter and scaling amplifier (SIM965, and SIM983 – Stanford Research Systems) to the fluid cell such that a negative voltage was applied to the patterned ITO-coated slide while the unpatterned ITO-coated slide was grounded. Images were taken using 5× magnification with camera exposure times that were chosen to be longer than the duration of the voltage applied to the fluid cell. Reference images were taken immediately preceding each measurement with the same camera exposure time. Analysis was conducted using ImageJ (National Institutes of Health). For display purposes, the brightness and contrast of all images were adjusted using the auto brightness contrast function with fine tune adjustments to the brightness and contrast done manually in ImageJ.

Results and Discussion

Optimization of reaction conditions

To determine whether ECL of luminol could be used to identify the location of electrically conductive regions on substrates, we performed an experiment in which an ITO-coated slide was patterned with photoresist to feature a 500 μm diameter exposed region. The fluid cell (Figures 1B and 1C) was subsequently filled with a pH 12 solution with 1 mM luminol and 5 mM H₂O₂. When viewed using bright field microscopy, the region without photoresist was clearly visible as a circle (Figure 1D). Upon the application of a 1.6 V DC voltage across the fluid cell for 2 s with no external illumination, bright ECL was observed centered on the exposed ITO circle with effectively no ECL intensity present in the insulating region outside the circle. Interestingly, the circle's border appeared slightly brighter, suggesting that phenomena such as diffusion influence the spatial uniformity of the ECL intensity. Indeed, such "edge effects" have been previously noted for ECL-based assays and attributed to non-uniform diffusion of reagents. 26 The presence of these edge effects suggests that while ECL may be easy to generate, converting this to a quantitative imaging approach may require further exploration.

While ECL was clearly visible in the conductive regions of the sample, it was not clear whether the chosen experimental conditions produced the largest ECL intensity or the degree to which processes such as reagent diffusion limited the spatial uniformity of the ECL signal. In order to study whether the solution composition affected these considerations, we defined a method for quantifying ECL intensity. In particular, the intensity with no voltage applied was denoted as a background intensity $\langle I_0 \rangle$ (Figure 2A). After applying a voltage, the average intensity inside the circular region was denoted $\langle I_V \rangle$. Note that the outer 15% of the circular region was omitted from this analysis to avoid contributions from the bright ring at the edge of the feature (Figure 2B).

With a quantitative measure of ECL intensity in hand, we sought to explore the influence of processing conditions on ECL intensity. Prior work has studied various factors, including pH,^{20–22} buffer composition,²¹ luminol concentration,^{20,21} and hydrogen peroxide concentration.²⁰ Thus, we tested the effects of each factor to determine the parameters that resulted in the highest ECL intensity. The buffer compositions and pHs tested included pH 10 sodium borate, pH 10 sodium bicarbonate, pH 11 sodium bicarbonate, and pH 12 disodium phosphate. Each buffer condition was studied with luminol concentrations between 0.1 and 10 mM (Figure 2C). Three key features emerged from this exploration. (1) The choice of buffer is imperative, with different buffers exhibiting more than a factor of 2 variation in ECL intensity with the same luminol

concentration at the same buffer pH. (2) Below 3.2 mM luminol, all buffers exhibited an increase in ECL intensity with increasing luminol concentration, which suggests that, in this concentration range, the reaction is diffusion limited. (3) At higher luminol concentrations, the ECL intensity was dependent on buffer composition, with some buffers leading to a decrease in ECL intensity at 10 mM luminol. These data are consistent with previous findings that show an optimal luminol concentration with higher concentrations leading to less ECL.^{20,21} This decrease in ECL with increasing luminol concentration has been attributed to electrode passivation at high luminol concentrations.^{21,27} Furthermore, it is well established that pH significantly affects ECL intensity with alkaline pHs resulting in increasingly higher signals until a threshold value where ECL signal decreases. 20-22,24 Therefore, the solution conditions expected that produced the highest ECL intensity were pH 11 sodium bicarbonate buffer with 3.2 mM luminol.

Having identified optimized buffer conditions and luminol concentrations, determining the optimal hydrogen peroxide concentration represented a balance between signal intensity and the robustness of the imaging method. In particular, it has been shown that high ECL intensity is observed with H_2O_2 in excess; $^{20,22-24}$ however, in our initial feasibility experiments, high concentrations of H_2O_2 led to bubble formation, which obscured optical imaging and, thus ECL signal. To optimize these competing considerations, ECL measurements were performed

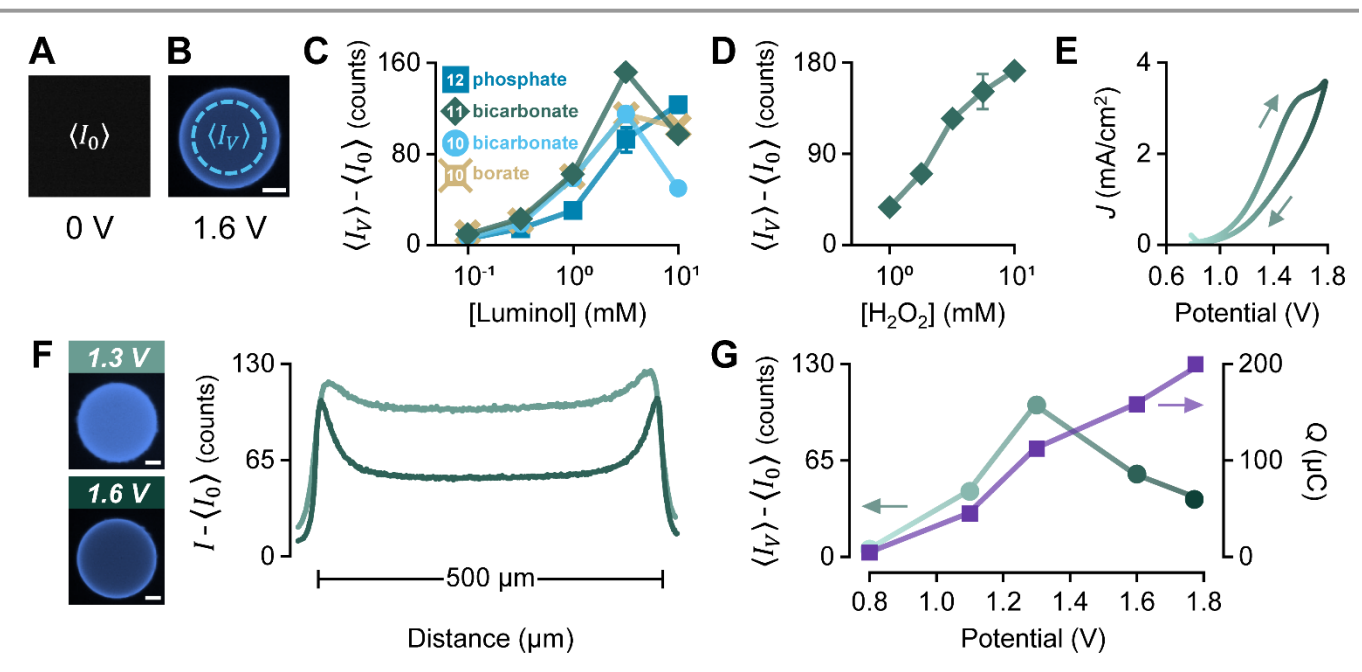


Fig. 2 (A) Optical micrograph through the electrochemical cell with no external illumination and no voltage applied. This image is used to define an average dark intensity $\langle I_0 \rangle$. (B) Optical micrograph through the electrochemical cell with no external illumination but applied voltage V=1.6 V. The bright circle corresponds to a 500 μm diameter region of exposed anode. The representative ECL intensity $\langle I_V \rangle$ is defined as the average intensity inside the dashed circle. (C) $\langle I_V \rangle - \langle I_0 \rangle$ vs. luminol concentration for four buffers with 5 mM hydrogen peroxide with V=1.6 V applied for duration t=2 s. Buffers studied are (12) pH 12 sodium phosphate, (11B) pH 11 sodium bicarbonate, (10) pH 10 sodium borate, and (10B) pH 10 sodium bicarbonate (full details in methods). (D) $\langle I_V \rangle - \langle I_0 \rangle$ vs. hydrogen peroxide concentration in bicarbonate buffer at pH 11 with 3.2 mM luminol with V=1.6 V and luminol and 5.6 mM hydrogen peroxide. (F) Micrograph intensity V=1.6 V as position shown for two experiments taken with different V=1.6 V and the substituting a buffer at pH 11 with 3.2 mM luminol and 5.6 mM hydrogen peroxide. Full optical micrographs are shown for each condition on the left. (G) $\langle I_V \rangle - \langle I_0 \rangle$ and total charge passed V=1.6 V taken simultaneously with V=1.6 V and luminol and 5.6 mM hydrogen peroxide. All scale bars are 100 μm. All micrograph images were taken in greyscale and false-colored to represent the color seen by eye. Error bars for (C) and (D) represent standard deviation of three trials using different cells and are smaller than markers if not visible.

with peroxide concentrations between 1 and 10 mM using the optimized luminol solution (3.2 mM luminol in pH 11 bicarbonate buffer). While the ECL intensity did increase with increasing peroxide concentration (Figure 2D), only a 14% increase was observed in going from 5.6 to 10 mM. This suggests that these concentrations represented a suitable excess concentration relative to luminol such that the peroxide was not substantially limiting the reaction. Thus, 5.6 mM $\rm H_2O_2$ was selected as a compromise to balance ECL intensity and bubble formation.

After establishing the optimal composition of the working solution, cyclic voltammetry (CV) was used to identify the functional voltage range for this solution composition and shed additional light on the electrochemical transformations taking place. Figure 2E shows a typical CV curve of a solution with $3.2\ mM$ luminol, $5.6\ mM\ H_2O_2$, in pH 11 bicarbonate buffer. A shoulder in the CV trace was observed at ~1.4 V, suggesting that the electrochemical reaction is mass-transfer limited at this voltage. This further suggests that additional oxidation is occurring at higher voltages, presumably the oxidation of hydrogen peroxide. To explore this reaction's relevance to ECL, we performed ECL imaging experiments on two samples, one collected with 1.3 V and the other with 1.6 V. While both exhibited bright circles of ECL, the center of the circular area was significantly dimmer in the sample at the higher voltage (shown in Figure 2F micrograph). To analyze the apparent ring in the image acquired at the higher voltage, the intensity profile I was computed along a 550 μm long line through the center of the circle by averaging the pixel values in a 15 μ m-wide region on either side of the line (Figure 2F). This analysis confirmed that not only did the 1.3 V image exhibit a higher average intensity in the circular region than the 1.6 V image, but that the edge effect was markedly less intense at the lower voltage.

In order to study the connection between the electrical and the optical signal more quantitatively, ECL experiments were performed at a series of five voltages while observing the charge passed using chronoamperometry (Figure 2G). Comparing the intensity with charge passed Q, intensity increased with voltage with voltages ≤ 1.3 V and then decreased with increasing voltage for > 1.3 V. Since Q monotonically increased with voltage, this indicates other electrochemical processes were taking place that inhibited ECL. Given that this experiment is taking place in the presence of hydrogen peroxide, hydrogen peroxide oxidation is an obvious candidate reaction. Furthermore, since the ring formation is more substantial in the presence of this competing reaction, it suggests the depletion of hydrogen peroxide is inhibiting ECL more strongly in the center region where diffusion is limited.

Considering that the voltage-dependent experiments suggest that light intensity is non-monotonically dependent upon reagent concentration and is influenced by secondary reactions, it is interesting to consider whether exploring the dynamics of ECL could allow one to find a balance between edge effects and signal intensity. To explore this, a series of experiments were performed in which the duration t over which the voltage was applied was varied from 10 ms to 30 s (Figure 3A). Interestingly, the intensity measured at 1.3 V

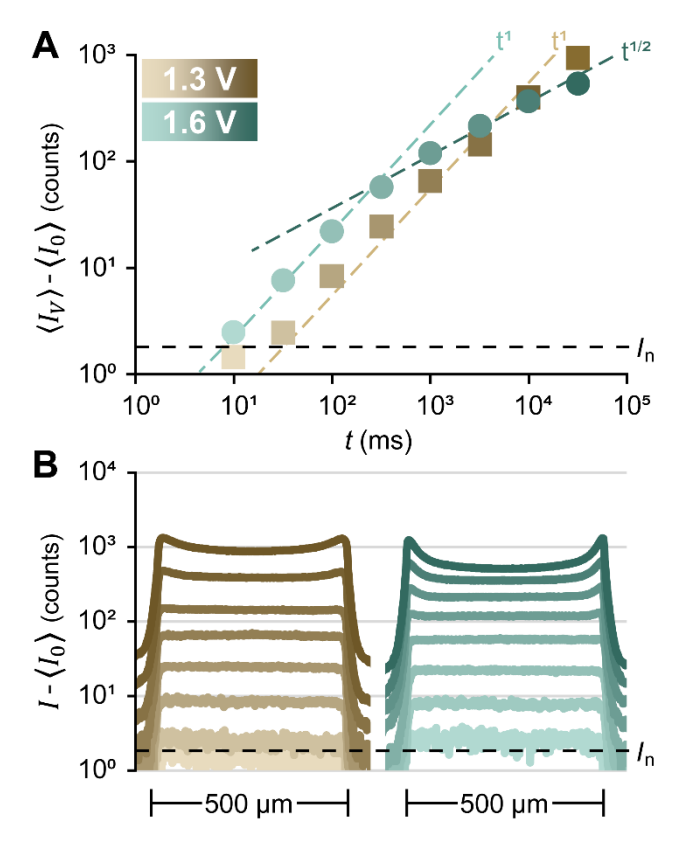


Fig. 3 (A) $\langle I_V \rangle - \langle I_0 \rangle$ vs. t for V=1.3 V (brown) and V=1.6 V (teal) of a bicarbonate buffer at pH 11 with 3.2 mM luminol and 5.6 mM hydrogen peroxide. The calculated noise (I_n) is indicated by the black dashed line. (B) Micrograph intensity $I-\langle I_0 \rangle$ vs. position shown for two experiments taken with different V of a bicarbonate buffer at pH 11 with 3.2 mM luminol and 5.6 mM hydrogen peroxide. Color saturation increases with increasing time as shown in (A).

increased nearly linearly once the signal was larger than the noise intensity I_n , defined as the standard deviation of the dark image. Such a linear increase in signal with time is what one would expect if the reaction were proceeding light in a timeinvariant fashion. In contrast, when measuring at 1.6 V, the signal drops below the linear power law at ~300 ms and adopts a $t^{1/2}$ power law, which is consistent with the reaction being limited by diffusion. These results suggest an explanation in which the 1.6 V process generates more ECL initially, but then shows a decrease in the rate of ECL generation due to hydrogen peroxide depletion at longer times, allowing a non-radiative luminol reaction to take precedence.28 The spatial profiles (Figure 3B) of these experiments are consistent with this mechanism, in which a deviation from the linear trend is accompanied by the presence of the edge effect. This ring can be explained as regions in which shorter diffusion is required to replenish the depleted hydrogen peroxide leading to higher ECL intensity. Further, this transition from uniform luminescence at low potentials to ring features at high potentials is consistent with a transition from reaction-limited to diffusion-limited regimes observed previously in dyes absorbing on circular patterned domains.²⁹ In the diffusion-limited regime, the dye concentration in the solution at the center of the circle was depleted while diffusion from areas outside the circle more rapidly replenished the dye concentration at the edge.

The results of the imaging and optimization experiments suggest a few important considerations for developing an ECL assay for defect detection. Critically, it is possible to choose conditions where local conductivity maps well to local ECL intensity. The best conditions for this are those in which the traces in Figure 3B are highest while still being flat, or 3.2 s at 1.3 V. That said if the goal is simply to generate the largest possible intensity so that small defects can readily be visualized, longer times can be used with 30 s at 1.3 V resulting in the highest absolute signal. Practically speaking, using as short a time as possible is still preferred in general, as shorter times will use up less reagent, potentially allowing more images to be taken while reducing the time needed for each measurement.

While the prior experiments had focused on large conductive regions as a tool to optimize the assay conditions, a major goal of this work is to identify small defects in otherwise insulating films. To explore whether ECL could be used to identify sub-micron conductive defects in electrically insulating films, we performed a series of experiments in which an ITO-coated slide was coated with insulating PMMA and patterned using electron beam lithography (EBL). As the characteristic defects of interest are pinholes and cracks, we studied both lines designed to be between 0.1 to 1 μm wide and circles designed to be between 0.1 to 1 μm in diameter. The final

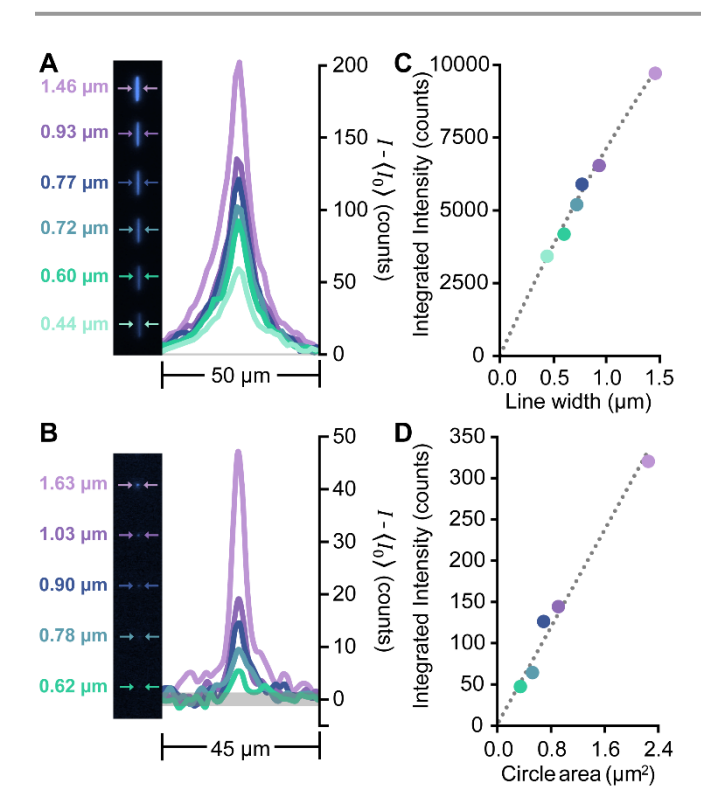


Fig. 4 (A) ECL micrograph of a line array and line cuts of the micrograph intensity $I-\langle I_0\rangle$ across each feature. ECL was carried out with V=1.3 V for t=10 s in a bicarbonate buffer at pH 11 with 3.2 mM luminol and 5.6 mM hydrogen peroxide. (B) ECL micrograph of circle array and line cuts of $I-\langle I_0\rangle$ across each feature. ECL was carried out with V=1.3 V for 10 s in a bicarbonate buffer at pH 11 with 3.2 mM luminol and 5.6 mM hydrogen peroxide. (C) Integrated intensity vs. line width calculated from the data in (A). (D) Integrated intensity vs circle area calculated from the data in (B). All micrograph images were taken in greyscale and false-colored to represent the color seen by eye. Grey bands in (A) and (B) represent the noise floor.

dimensions of these lines and dots were measured using SEM and found to be between 0.44 - 1.46 μm wide and between 0.62 - 1.63 μm in diameter, respectively. ECL was performed on these samples using the optimized reagents, V=1.3 V, and t=10 s. The results of these ECL studies for both the line and dot features are shown in Figure 4A and Figure 4B as both ECL images and line cuts. All features were found to provide a clear optical signal with the shape of the ECL image matching the patterned shape.

While our lithography system was not readily capable of patterning substantially smaller features than those explored in Figures 4A and 4B, we hypothesized that these experiments could allow us to estimate the smallest features that would be possible to identify using this approach. In particular, we computed the average ECL intensity by integrating the intensity in a 10 µm square centered on each feature. Plotting this integrated intensity vs. line width (Figure 4C) revealed a monotonic increase in intensity with increasing line width in a linear manner for lines narrower than 1 μm . Extrapolating to calculate the minimum resolvable line as the point where this fit line crosses the noise floor, we estimate that lines as narrow as 2.5 nm should be resolvable under these conditions. To estimate the minimum resolvable circular features, we integrated the intensity in a 5 µm circle centered on the dot of interest and found that this was highly linear with the dot area (Figure 4D), as one would expect. Extrapolating this curve to smaller areas, we find that circles with a radius of 70 nm should be the smallest resolvable features. For both the line and circle features, the background noise was estimated by calculating the integrated intensity in 15 different regions where no features were present in the ECL image and then subtracting the dark current (i.e., integrated intensity from when no voltage is applied). This led to lines having a noise of ~20 counts and circles having a noise of 2.5 counts. Interestingly, when considering that the area of the sample interrogated by a single pixel of the camera is 1290 × 1290 nm² at 5× magnification, the area of the minimum resolvable line and circle features occupy similar fractions of this area, with dots taking up 1/100 and lines $\,$ taking up 1/516 of the area. While these ratios being on the same order of magnitude suggests that the quantity of ECL generated is proportional to the exposed area, the difference in intensity between lines and circles suggests either a more prominent role of diffusion or differences in residual electron beam resist between line and circle features, as is evident in the SEM images of the features (Figures S1 and S2).

To explore the degree to which this assay could be used to provide insight about defects on nominally insulating films, we captured a series of ECL images on a 7.2 × 3.2 mm² region of an ITO-coated glass slide onto which an ultrathin layer of dielectric poly(phenylene oxide) had been electrodeposited.³0 These and similar ultrathin functional coatings have recently been shown to be of interest for advanced energy technologies.³,31 As this region was much larger than the region corresponding to the microscope's field of view, this imaging task was completed by iteratively taking ECL images and then moving the microscope stage. The motion was performed manually while accounting for a 10-20% areal overlap between neighboring frames to

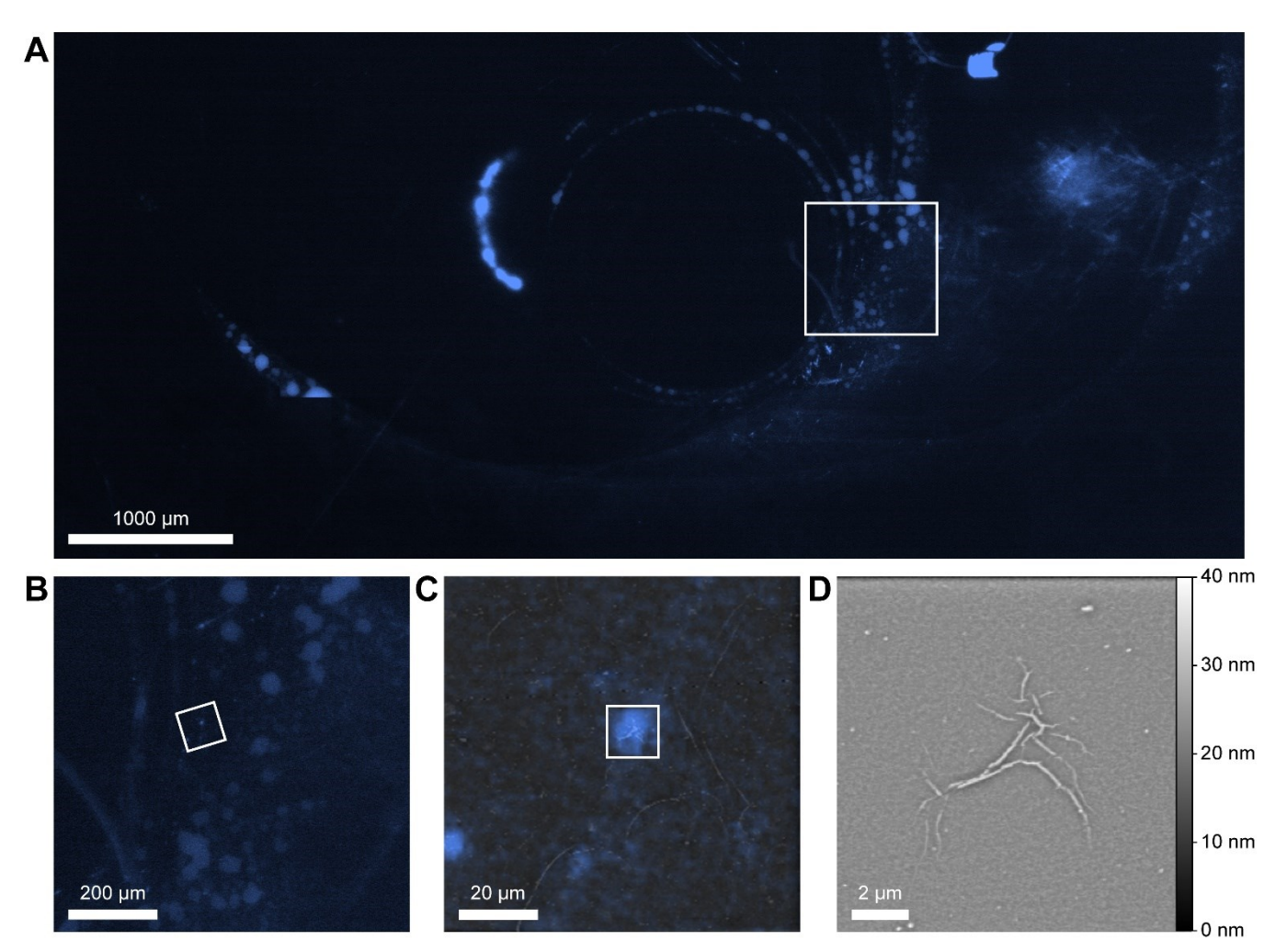


Fig. 5 (A) Composite ECL micrograph of a phenol film taken with $5\times$ objective, camera exposure 12 s, with 3.2 mM luminol, 5.6 mM H_2O_2 , in pH 11 bicarbonate buffer with an applied potential of 1.3 V for 10 s for each frame. (B) Magnified view of the noted region in (A) showing a region of interest for further characterization. (C) Magnified and rotated view of the noted region in (B) overlaid on an AFM topographical image of the same location. (D) AFM topographical image corresponding to the noted region in (C). All ECL micrographs were taken in greyscale and false-colored to represent the color seen by eye.

facilitate stitching the images together. Each ECL image was collected by applying 1.3 V for 10 s. The resulting images were stitched together to create a composite (Figure 5A).

Examining the large-area composite ECL of the phenol film, a few features were immediately apparent that provided important feedback for synthesis. First, it was clear that the film had several large defects, including circular bands that were tens of microns wide. While these features were not visible in bright or dark-field optical microscopy, their circular shape leads us to believe that they were related to the process of solvent drying on the sample surface. Analysis of the substrate preparation, film synthesis, and subsequent electrodeposition led us to conclude that the cleaning procedure used for substrate preparation was inadequate.

While the large-scale information that stemmed from the whole image is important and can provide a unique window into optimizing the deposition process, understanding the origin of individual defects is equally important. Specifically, we sought to test whether bright spots in ECL could be linked to their nanoscale morphology to identify the structural origin of a defect. To explore this, we identified a region of interest

(Figure 5B) with a particularly bright spot and colocalized this region using AFM through a combination of optically visible imperfections on the film surface as fiducial marks in addition to a grid system that was attached to the back of the sample. After locating the region of interest by taking several large format AFM images onto which the ECL images can be overlaid (Figure 5C), we performed a topographic image of the bright spot in the center of the region of interest. Interestingly, this $13 \times 13 \ \mu m^2$ AFM image revealed a cluster of sub-micron wrinkles in the film with prominent ridges between 100 -250 nm in width (Figure 5D). This zoomed-in image suggests that this defect is not a large region that wasn't deposited or a piece of dirt that prevented deposition but rather a result of film overgrowth or swelling leading to buckling on the film surface. While the presence of folds does not itself explain why the film is conductive, two possibilities seem plausible. First, the folds themselves could be cracks, especially in regions where two lines meet at a right angle, which is a hallmark of cracking.32 Alternatively, if there was a small conductive defect during electrodeposition, this could have led to local compressive stresses on the film, which could produce a blister that results

in a circular domain of folds, similar to what is observed here.³³ The main virtue of the ECL assay in this case is to draw attention to this region of the film to motivate further study into the precise mechanism of defect formation. This type of information can provide insight into defect formation and feedback for synthesis optimization.

The process of conducting a large-area scan on a nominally insulating film demonstrates the key utility of this ECL imaging method as a rapid approach for identifying small defects in large areas. Significantly, the ability to colocalize ECL features with AFM images provides flexibility to study families of defects efficiently. For example, using our AFM system's maximum field of view (90 \times 90 μ m²) to complete scans across the entire region imaged by ECL would have required scanning an area of $23,040,000 \, \mu m^2 \, \text{or} > 2,800 \, \text{scans}$. Not considering the burden of processing the data collected, the time needed to complete the experiment itself would exceed 900 hours. For comparison, the same area scanned using the optimized luminol-based ECL assay developed in this work required 18 ECL images and 18 reference images, with a camera exposure time of 12 s for each image and 30 s between voltage applications to allow equalization of reagents through diffusion, resulting in data collection within 20 minutes. Perhaps most importantly, even if the tedious AFM characterization was performed, it would not be obvious which defects were conductive, while ECL imaging directly measures the functional property of interest. It is worth considering specific workflows in which this ECL-based method could provide feedback to synthesis. We envision an iterative process wherein films of interest are initially screened using electrical impedance spectroscopy (EIS) over a large area to obtain an estimate of the average conductivity of the entire film. Then, regions of the film can be studied using ECL to determine the homogeneity and intensity of conductivity. Specifically, there are many reasons why a film may appear conductive to EIS, entire regions could be missing or incomplete, cracks could have formed post synthetically, or pinholes can be present across the sample. Inspection of the ECL images can readily distinguish between these phenomena. Furthermore, regions of interest can be identified, such as features with optical contrast in bright- or dark-field imaging, and these could be subjected to local high-resolution ECL to identify these regions as conductive or superficial defects. As far as how this information is used synthetically, if the film is nonuniform in its imperfections, this implicates processing conditions such as substrate cleaning or reactor uniformity.

Conclusions

Taken together, we have developed a novel method for detecting sub-micron defects in insulating thin films using low-resolution tools. We systematically studied reagent concentrations, voltages, and excitation time, allowing us to optimize reaction conditions. While luminol concentration, buffer composition, pH, and excitation voltage can be optimized to find a maximum signal, hydrogen peroxide concentration and excitation monotonically influence ECL signal but present tradeoffs in other ways. Specifically, excess hydrogen peroxide

leads to bubble formation, while prolonged measurement leads to diffusion-based edge effects. This optimization directly improves the resolving power of this analytical method. Using extensive signal-to-background measurements of sub-micron features, we predict that lines as narrow as 2.5 nm and pinholes as small as 70 nm in radius should be in principle detectable. Additionally, we show multi-image stitching and co-registered mapping of nanoscale defects covering a >20 mm² sample. We note that the one factor at a time-based optimization performed here is not able to capture cross-interactions in a single pass. As such, full-factorial design of experiments or alternative iterative optimization strategies such as Bayesian optimization could be used to further improve signal intensity.34 Given the emergence of self-driving labs as platforms to rapidly optimize complex systems, we expect such systems to both drive and facilitate this optimization in formats that are amenable to automation.³⁵ Collectively, these results show that this ECL imaging can be used to rapidly screen nominally insulating films for nanoscale defects, a critical capability for confident application of advanced materials in stretchable electronics, conformal coatings, and photovoltaic devices. Given the optical nature of this measurement, it can be readily combined with other non-destructive techniques for characterizing functional films. Further, this assay is inherently parallelizable and thus amenable to incorporation in an automated process for high-throughput screening of multifunctional films.

Author Contributions

Harley Quinn: data curation, formal analysis, investigation, methodology, writing – original draft, and visualization. Wenlu Wang: investigation and writing – review and editing. Jörg G. Werner: conceptualization, funding acquisition, supervision, and writing – review and editing. Keith A. Brown: conceptualization, funding acquisition, project administration, supervision, and writing – original draft.

Conflicts of interest

There are no conflicts to declare.

Acknowledgements

This work was supported by the National Science Foundation (CBET-2146597) and the Boston University College of Engineering Dean's Catalyst Award. The authors are grateful to the Boston University Photonics Center for providing access to instrumentation and resources critical to this work.

References

- G. Chasta, Himanshu and M. S. Dhaka, *Int. J. Energy Res.*, 2022, 46, 14627–14658.
- N. J. Dudney, *Mater. Sci. Eng. B*, 2005, **116**, 245–249.
- 3 J. G. Werner, G. G. Rodríguez-Calero, H. D. Abruña and U.

- Wiesner, Energy Environ. Sci., 2018, 11, 1261–1270.
- 4 S. Moitzheim, B. Put and P. M. Vereecken, *Adv. Mater. Interfaces*, 2019, **6**, 1900805.
- 5 S. Oukassi, L. Baggetto, C. Dubarry, L. Le Van-Jodin, S. Poncet and R. Salot, *ACS Appl. Mater. Interfaces*, 2019, **11**, 683–690.
- G. Yang, C. Abraham, Y. Ma, M. Lee, E. Helfrick, D. Oh and D. Lee, Appl. Sci.
- M. Li, F. Igbari, Z. Wang and L. Liao, *Adv. Energy Mater.*, 2020, **10**, 2000641.
- 8 F. Liu, Q. Zeng, J. Li, X. Hao, A. Ho-Baillie, J. Tang and M. A. Green, *Mater. Today*, 2020, **41**, 120–142.
- G. Benstetter, R. Biberger and D. Liu, *Thin Solid Films*, 2009,
 517, 5100–5105.
- V. V. Korolkov, A. Summerfield, A. Murphy, D. B. Amabilino,
 K. Watanabe, T. Taniguchi and P. H. Beton, *Nat. Commun.*,
 2019, 10, 1–8.
- P. Panjan, A. Drnovšek, P. Gselman, M. Čekada and M. Panjan, *Review of growth defects in thin films prepared by PVD techniques*, 2020, vol. 10.
- 12 A. Sirman, F. Al-Amoody, C. Palamadai, B. Saville, A. Jain and K. Tran, *ASMC (Advanced Semicond. Manuf. Conf. Proc.*, 2019, **2019-May**, 420–424.
- T. Maerten, C. Jaoul, R. Oltra, P. Duport, C. Le Niniven, P. Tristant, F. Meunier and O. Jarry, C J. Carbon Res., 2019,
 73
- 14 V. Ruiz, P. Liljeroth, B. M. Quinn and K. Kontturi, *Nano Lett*, 2003, **3**, 1459–1462.
- J. Azevedo, C. Bourdillon, V. Derycke, S. Campidelli, C. Lefrou and R. Cornut, Anal. Chem, 2012, 85, 1812–1818.
- 16 R. Kempaiah, G. Vasudevamurthy and A. Subramanian, *Nano Energy*, 2019, **65**, 103925.
- 17 S. K. Sia, V. Linder, B. A. Parviz, A. Siegel and G. M. Whitesides, *Angew. Chemie Int. Ed.*, 2004, **43**, 498–502.
- S. Xu, Y. Liu, T. Wang and J. Li, Anal. Chem, 2011, 83, 3817–3823.
- 19 Y. K. Cho, H. Kim, A. Bénard, H. K. Woo, F. Czubayko, P. David, F. J. Hansen, J. I. Lee, J. H. Park, E. Schneck, G. F. Weber, I. S. Shin and H. Lee, *Sci. Adv.*, 2022, **8**, 1–11.
- Y. Lin, H. Dai, G. Xu, T. Yang, C. Yang, Y. Tong, Y. Yang and
 G. Chen, *Microchim. Acta*, 2013, **180**, 563–572.
- 21 C. A. Marquette, B. D. Leca and L. J. Blum, *Luminescence*, 2001, **16**, 159–165.
- 22 N. Wint, Z. S. Barrett, G. Williams and H. N. McMurray, *J. Electrochem. Soc.*, 2019, **166**, C3417–C3430.
- 23 H. Zhu, D. Jiang and J.-J. Zhu, *Chem. Sci.*, 2021, **12**, 4794–4799.
- 24 S. Hu, Z. Cao, L. Zhou, R. Ma and B. Su, J. Electroanal. Chem., 2020, 870, 114238.
- A. Rendos, W. Cao, M. Chern, M. Lauricella, S. Succi, J. G. Werner, A. M. Dennis and K. A. Brown, *Soft Matter*, 2022, **18**, 1991–1996.
- D. J. Walton, S. S. Phull, D. M. Bates, J. P. Lorimer and T. J. Mason, *Electrochim. Acta*, 1993, **38**, 307–310.
- C. M. Geiselhart, C. Barner-Kowollik and H. Mutlu, *Polym. Chem.*, 2021, 12, 1732–1748.
- J. E. Vitt, D. C. Johnson and R. C. Engstrom, J. Electrochem.

- Soc., 1991, 138, 1637-1643.
- K. M. Carroll, A. W. Knoll, H. Wolf and U. Duerig, *Langmuir*, 2018, 34, 73–80.
- 30 R. L. McCarley, E. A. Irene and R. W. Murray, *J. Phys. Chem.*, 1991, **95**, 2492–2498.
- 31 W. Wang, Z. Zheng, A. B. Resing, K. A. Brown and J. G. Werner, *Mol. Syst. Des. Eng.*, , DOI:10.1039/d2me00246a.
- 32 L. Weh and A. Venthur, *Macromol. Mater. Eng.*, 2004, **289**, 227–237.
- 33 K. Xie, A. Glasser, S. Shinde, Z. Zhang, J. M. Rampnoux, A. Maali, E. Cloutet, G. Hadziioannou and H. Kellay, *Adv. Funct. Mater.*, 2021, **31**, 1–9.
- 34 B. Cao, L. A. Adutwum, A. O. Oliynyk, E. J. Luber, B. C. Olsen, A. Mar and J. M. Buriak, ACS Nano, 2018, 12, 7434–7444.
- E. Stach, B. DeCost, A. G. Kusne, J. Hattrick-Simpers, K. A.
 Brown, K. G. Reyes, J. Schrier, S. Billinge, T. Buonassisi, I.
 Foster, C. P. Gomes, J. M. Gregoire, A. Mehta, J. Montoya,
 E. Olivetti, C. Park, E. Rotenberg, S. K. Saikin, S. Smullin, V.
 Stanev and B. Maruyama, *Matter*, 2021, 4, 2702–2726.